frontiers in Earth Science

ORIGINAL RESEARCH
published: 25 November 2021
doi: 10.3389/feart.2021.782901

Imaging Complex Subsurface Structures for Geothermal Exploration at Pirouette Mountain and Eleven-Mile Canyon in Nevada

Yunsong Huang[1], *Miao Zhang*[1], *Kai Gao*[1], *Andrew Sabin*[2] *and Lianjie Huang*[1]*

[1]*Los Alamos National Laboratory, Geophysics Group, Los Alamos, NM, United States,* [2]*Navy Geothermal Program Office, China Lake, CA, United States*

OPEN ACCESS

Edited by:
Zhihui Zou,
Ocean University of China, China

Reviewed by:
Yike Liu,
Key Laboratory of Oil and Gas Resources Research, Institute of Geology and Geophysics (CAS), China
Bin He,
University of Toronto, Canada

***Correspondence:**
Lianjie Huang
ljh@lanl.gov

Specialty section:
This article was submitted to Solid Earth Geophysics, a section of the journal Frontiers in Earth Science

Received: *24 September 2021*
Accepted: *02 November 2021*
Published: *25 November 2021*

Citation:
Huang Y, Zhang M, Gao K, Sabin A and Huang L (2021) Imaging Complex Subsurface Structures for Geothermal Exploration at Pirouette Mountain and Eleven-Mile Canyon in Nevada. Front. Earth Sci. 9:782901. doi: 10.3389/feart.2021.782901

Accurate imaging of subsurface complex structures with faults is crucial for geothermal exploration because faults are generally the primary conduit of hydrothermal flow. It is very challenging to image geothermal exploration areas because of complex geologic structures with various faults and noisy surface seismic data with strong and coherent ground-roll noise. In addition, fracture zones and most geologic formations behave as anisotropic media for seismic-wave propagation. Properly suppressing ground-roll noise and accounting for subsurface anisotropic properties are essential for high-resolution imaging of subsurface structures and faults for geothermal exploration. We develop a novel wavenumber-adaptive bandpass filter to suppress the ground-roll noise without affecting useful seismic signals. This filter adaptively exploits both characteristics of the lower frequency and the smaller velocity of the ground-roll noise than those of the signals. Consequently, this filter can effectively differentiate the ground-roll noise from the signal. We use our novel filter to attenuate the ground-roll noise in seismic data along five survey lines acquired by the U.S. Navy Geothermal Program Office at Pirouette Mountain and Eleven-Mile Canyon in Nevada, United States. We then apply our novel anisotropic least-squares reverse-time migration algorithm to the resulting data for imaging subsurface structures at the Pirouette Mountain and Eleven-Mile Canyon geothermal exploration areas. The migration method employs an efficient implicit wavefield-separation scheme to reduce image artifacts and improve the image quality. Our results demonstrate that our wavenumber-adaptive bandpass filtering method successfully suppresses the strong and coherent ground-roll noise in the land seismic data, and our anisotropic least-squares reverse-time migration produces high-resolution subsurface images of Pirouette Mountain and Eleven-Mile Canyon, facilitating accurate fault interpretation for geothermal exploration.

Keywords: anisotropic least-squares reverse-time migration, imaging, geothermal exploration, ground-roll suppression, fault, complex structure

INTRODUCTION

The geothermal exploration areas at Pirouette Mountain and Eleven-Mile Canyon are located near the margins of Dixie Valley in Nevada, United States. Eleven-Mile Canyon lies next to the surface rupture terminations of 1954 Fairview Peak—Dixie Valley earthquake sequence (Caskey et al., 1996). The area contains a complex network of steeply-dipping faults and fractures, which creates the highly permeable fractures for the potential production zone at 2–3 km in depth (Unruh et al., 2016). It is crucial to accurately image and delineate subsurface fracture/fault zones for geothermal exploration and optimizing well placement, because faults/fracture zones provide paths for hydrothermal flow, but they may also be effective barriers to geothermal flow in some situations (Ba et al., 2015). It is particularly challenging to accurately image the subsurface structures at Pirouette Mountain and Eleven-Mile Canyon because of complex heterogeneities and possible anisotropies in both fracture zones and geologic formations.

In 2013, the U.S. Navy Geothermal Program Office carried out a seismic reflection survey (Alm et al., 2016) along five lines to evaluate the geothermal potential at Pirouette Mountain and Eleven-Mile Canyon, NV. Lines 1, 2, 3, and 4 were aligned west-east to cross the valley, while Line 5 was placed along a north-south trend to intersect Lines 1–3 (**Figure 1**). Lines 1, 2, 3, and 5 are located at Pirouette Mountain, and Line 4 is at Eleven-Mile Canyon. Such a geometry of the survey aimed to allow enhanced horizon and fault interpretations.

For imaging complex subsurface structures at Pirouette Mountain and Eleven-Mile Canyon, we first need to properly suppressing ground-roll noise in the acquired seismic data.

Ground-roll noise refers to high-amplitude and coherent surface waves (Sheriff, 2002), which not only provide little information regarding deeper reflectors of interest, but also contaminate subsequent geophysical imaging, particularly for waveform inversion and least-squares reverse-time migration that are based on waveform fitting. Although Rayleigh waves dominate ground-roll noise, the latter may also include Love waves, reverberated refractions, and waves scattered by near-surface heterogeneities. Ground-roll noise often masks shallow reflections at near offsets and deep reflections at far offsets. This problem is acute for land

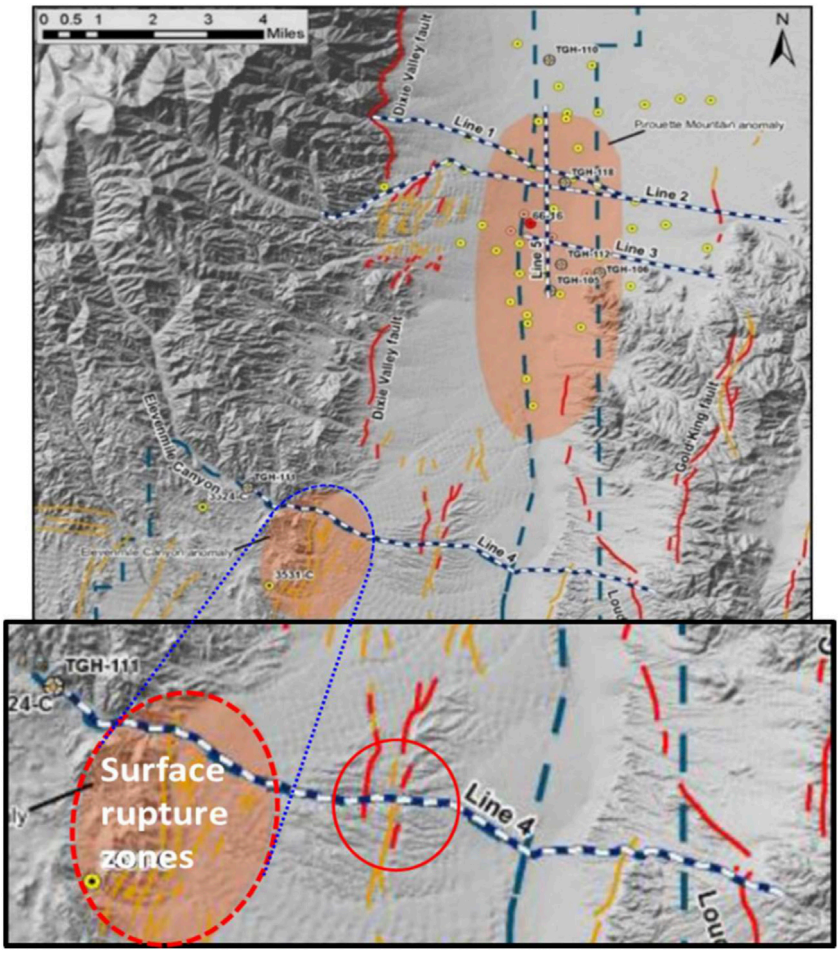

FIGURE 1 | Location map of the geothermal exploration areas at Pirouette Mountain and Eleven-Mile Canyon in southern Dixie Valley, Nevada, with five lines of seismic survey depicted in rails. The faults shown are from the U.S. Geological Survey Quaternary fault and fold database. Surface rupture zones correspond to the 1954 earthquake sequence (Unruh et al., 2016). The northern shaded region is at Pirouette Mountain, and the southern shaded region is at Eleven-Mile Canyon.

surface seismic data acquired at Pirouette Mountain and Eleven-Mile Canyon for geothermal exploration.

Because of near-surface layers and unconsolidated weathering zones, ground-roll noise propagates more slowly and exhibits lower frequency than do seismic reflections. A simple method to reduce ground-roll noise is therefore to apply a low-cut filter.

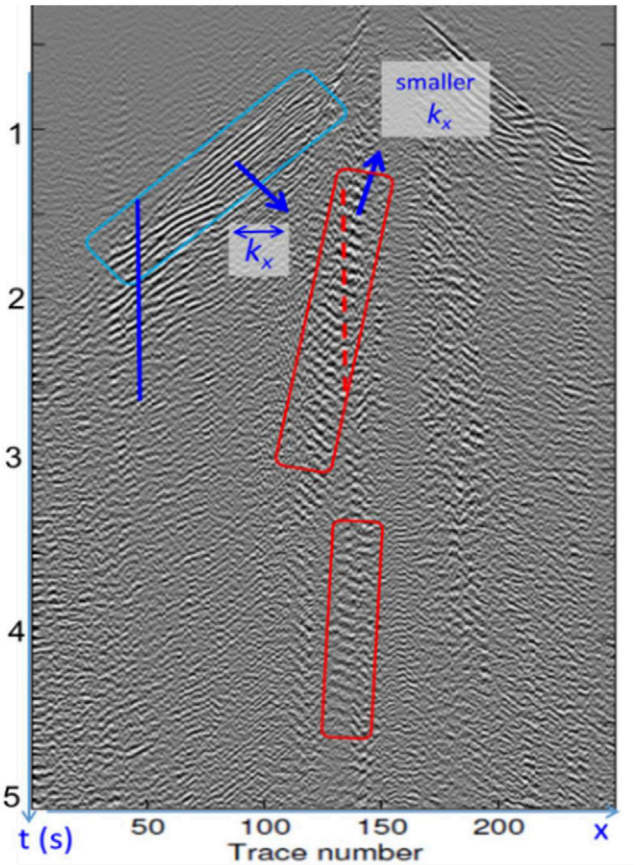

FIGURE 2 | A representative common-shot gather of surface seismic data. Red rectangles enclose the ground-roll noise. The cyan rectangle encloses reflection signals. The vertical red dashed line and blue solid line stride across the ground-roll noise and reflection signals, respectively. The single-barbed arrows indicate the wavenumber directions.

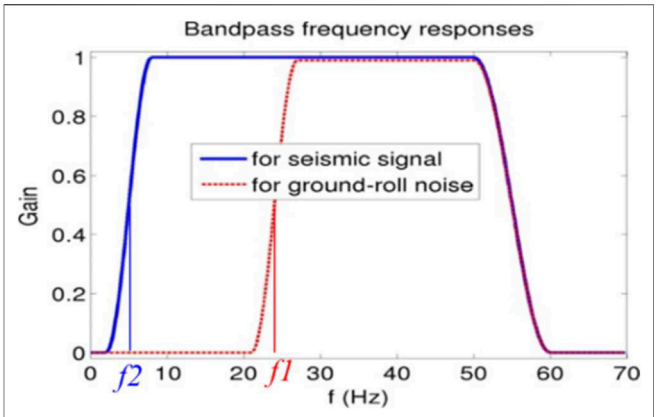

FIGURE 4 | If the input data are likely seismic signals, a bandpass filter with low cut-off frequency f_2 is preferable. Otherwise, a bandpass filter with a relatively high cut-off frequency f_1 is used to reject the ground-roll noise, of which the spectrum lies below f_1.

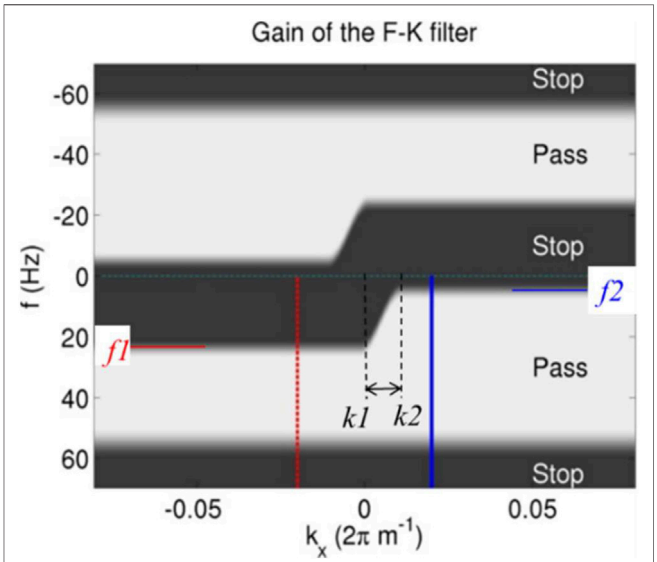

FIGURE 5 | Illustration of the new wavenumber-adaptive bandpass filter for seismic traces on the left side of the shot in a common-shot gather. The vertical slices along the blue and red lines yield the bandpass profiles in **Figure 4**. The cut-off frequencies f_1 and f_2 take the same values as in **Figure 4**.

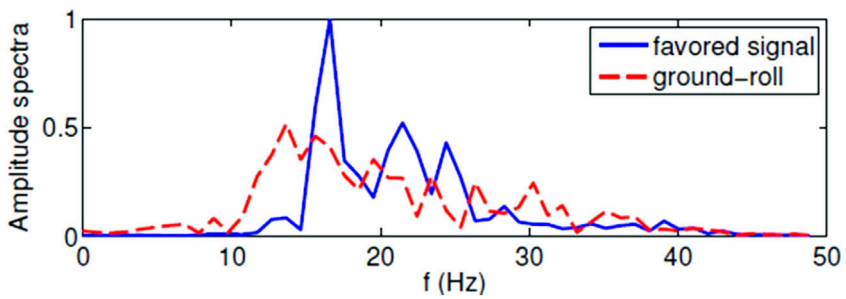

FIGURE 3 | The spectra of the ground-roll noise (red) and the reflection signal (blue).

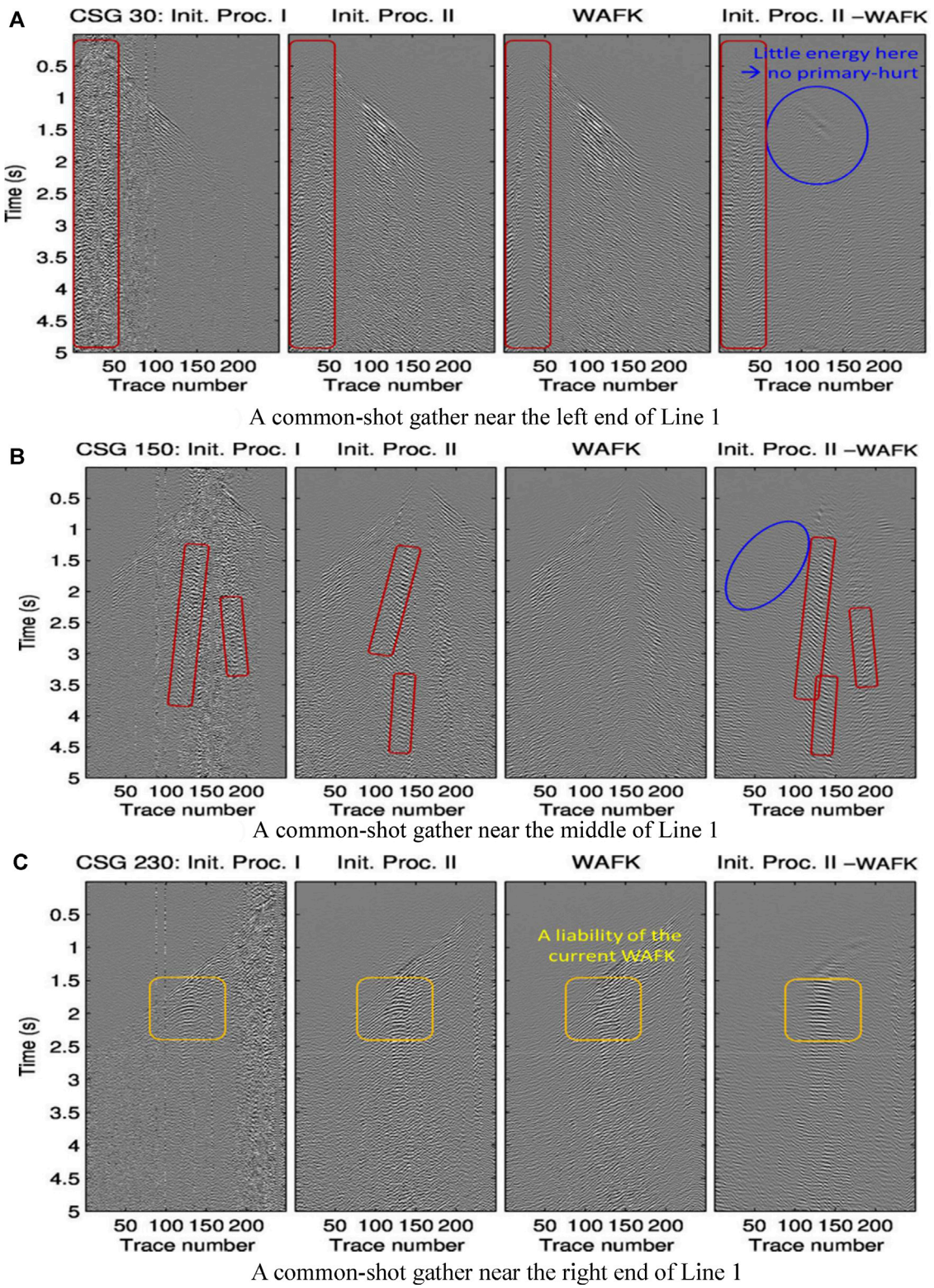

FIGURE 6 | Three common-shot gathers (CSGs 30, 150, and 230) corresponding to the three shots along Line 1: **(A)** CSG near the left end, **(B)** CSG around the middle, and **(C)** CSG near the right end of Line 1. The leftmost column shows an industry-processed data. The column titled "Init. Proc. II" presents the other industry-processed data. Our wavenumber-adaptive F-K filter (WAFK) operates upon this column, yielding results shown in column "WAFK." The rightmost column shows the difference between the inputs and outputs of WAFK. **(A)** A common-shot gather near the left end of Line 1. **(B)** A common-shot gather near the middle of Line 1. **(C)** A common-shot gather near the right end of Line 1.

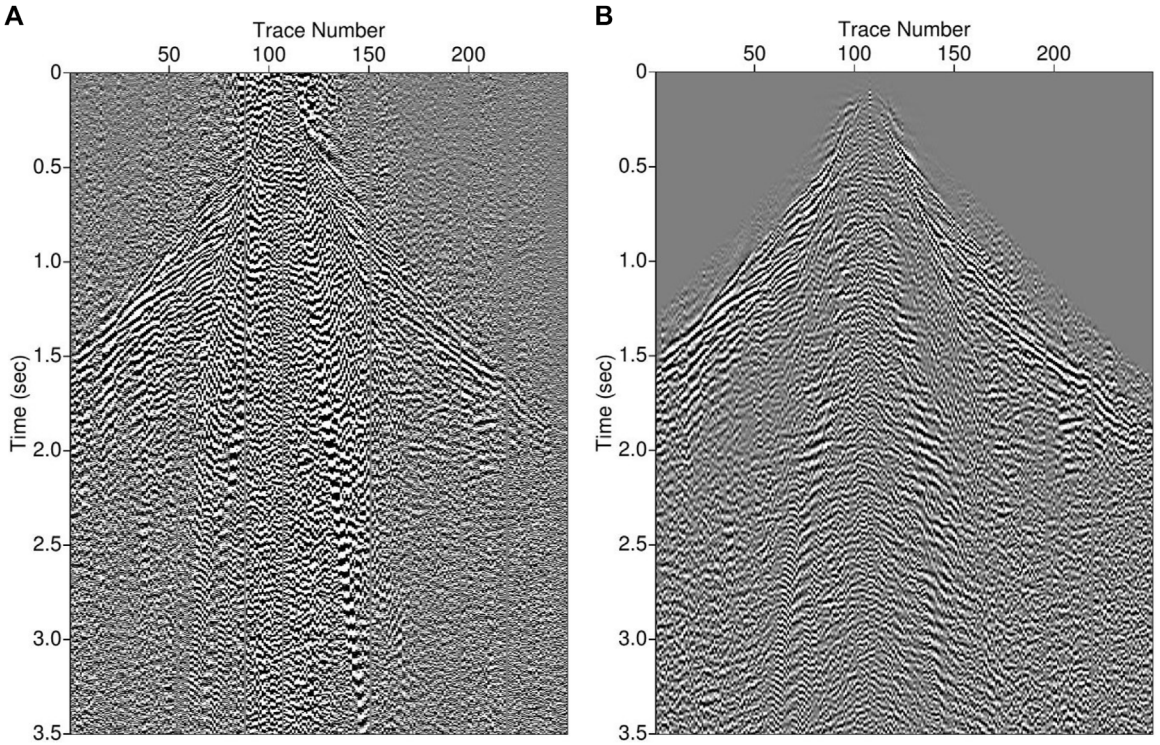

FIGURE 7 | Another example of a common-shot gather from Pirouette Mountain and Eleven-Mile Canyon before **(A)** and after **(B)** wavenumber-adaptive bandpass filtering. Waveforms before first arrivals in the right panel are muted with a cosine taper near the first arrivals. Coherent subsurface reflections become visible after filtering.

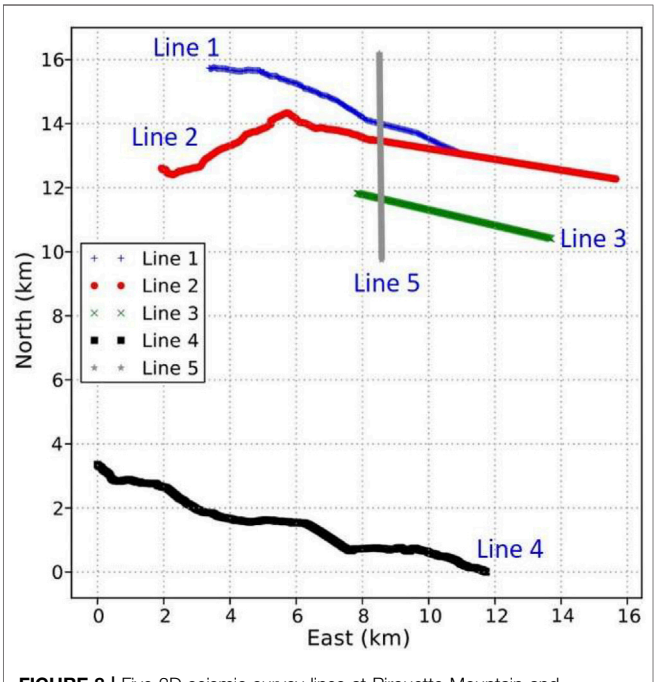

FIGURE 8 | Five 2D seismic survey lines at Pirouette Mountain and Eleven-Mile Canyon, Nevada, United States.

Unfortunately, this method also eliminates the low-frequency part of seismic reflection data, which is critical to waveform inversion and least-squares reverse-time migration.

Several methods were developed to suppress the ground-roll noise over the past several decades. A common motivation is to express the signal and the noise in a certain transform domain that helps separate the signal from the noise. A number of filtering methods were designed (Shieh and Herrmann, 1990), but the reflection data within the frequency bands overlapping with those of the noise could be filtered out (Coruh and Costain, 1983). One of techniques in the transform domain uses *f-k* filtering (Embree et al., 1963; Treitel et al., 1967; Yilmaz, 2001). Radon, or τ-p, transform was also applied to ground-roll noise suppression (Brysk and McCowan, 1986; Henley, 2003). Sparse Radon transforms (Trad et al., 2003) produce sparse representations of the signal and noise in the transform domain, thereby facilitating signal and noise separation. Challenges exist, however, when the moveout of seismic signals in a common-shot gather is irregular because of irregularities in the surface topography and weathering zones. Other techniques for suppressing the ground-roll noise include interferometry (Halliday, 2011), Karhunen–Loève (K–L) transform (Liu, 1999), singular value decomposition (SVD) (Jin and Ronen, 2005), wavelet transform (Deighan and Watts, 1997), and Wiener filtering (Karsli and Bayrak, 2008).

We develop a novel method to suppress the ground-roll noise without affecting reflection data. To distinguish the ground-roll noise from the signal, we exploit the information of the frequency content, wavenumber, and the relative offset in seismic data. Ground-roll noise exhibits dispersion, resulting in shingled events. The dip of each individual event lies opposite to those of reflections. This observation allows us to design a bandpass filter that is adaptive to wavenumber to fulfill our aim of ground-roll noise suppression.

After suppressing ground-roll noise in the seismic data acquired at Pirouette Mountain and Eleven-Mile Canyon using our novel wavenumber-adaptive bandpass filter, we can use the data to image subsurface structures and faults for geothermal exploration.

Reverse-time migration (RTM) is a powerful tool for imaging complex subsurface structures. In essence, RTM relocates the wave energy in seismic data to subsurface reflectors where the seismic waves are reflected before reaching seismic receivers at the surface for a surface seismic survey. Such a relocation of seismic-wave energy relies on numerical simulations of seismic-wave forward and backward propagation. When the subsurface media are anisotropic, as are typical in complex geothermal exploration fields (Gao and Huang, 2015), it is crucial to properly account for the subsurface anisotropic properties to allow accurate simulations of seismic wavefields. Anisotropic RTM can account for anisotropy for high-resolution subsurface imaging of complex structures with faults.

While RTM performs wave-energy relocation non-iteratively, an extension of RTM is termed least-squares RTM (LSRTM) (Nemeth et al., 1999), which iteratively adjusts the subsurface reflectors so that synthetic seismic data would maximally resemble (in the sense of least-squares residue) real seismic data. Because of ambiguity in the velocity model and limited numbers of sources and receivers, the non-iterative RTM suffers from migration artifacts. By contrast, because of the feedback control mechanism in the iterative LSRTM, the discrepancy between the imaged reflectors and the physical reflectors is restrained.

We apply our anisotropic least-squares reverse-time migration algorithm to the seismic data acquired at the Pirouette Mountain and Eleven-Mile Canyon geothermal exploration areas for reliable imaging of the complex subsurface structures with faults. First, we use our wavenumber-adaptive bandpass filter to suppress the ground-roll noise of the five 2D lines of surface seismic data acquired at Pirouette Mountain and Eleven-Mile Canyon. Then we apply our anisotropic LSRTM to the resulting data to obtain high-resolution subsurface images, and compare the images with industrial images and those obtained using anisotropic RTM.

We organize our paper as follows. We first introduce the methodology of our wavenumber-adaptive bandpass filter and anisotropic least-squares reverse-time migration, present results of ground-roll suppression using our wavenumber-adaptive bandpass filter, give anisotropic LSRTM images with comparison with industrial images and those obtained using anisotropic RTM images, and draw our findings in the Conclusion section.

METHODOLOGY

We present the methodology of our novel wavenumber-adaptive bandpass filter for suppressing the ground-roll noise, and our anisotropic least-squares reverse-time migration below.

Wavenumber-Adaptive Bandpass Filter

In a typical common-shot gather of surface seismic data, the ground-roll noise appears to be coherent and energetic (**Figure 2**). **Figure 3** shows spectra of two temporal slices of the reflection signals (blue line in **Figure 2**) and the ground-roll noise (red dashed line in **Figure 2**). Although the ground-roll noise is of lower frequency compared with the signal, it is evident that there is much overlap between the frequency bands of the signal and the noise. Note

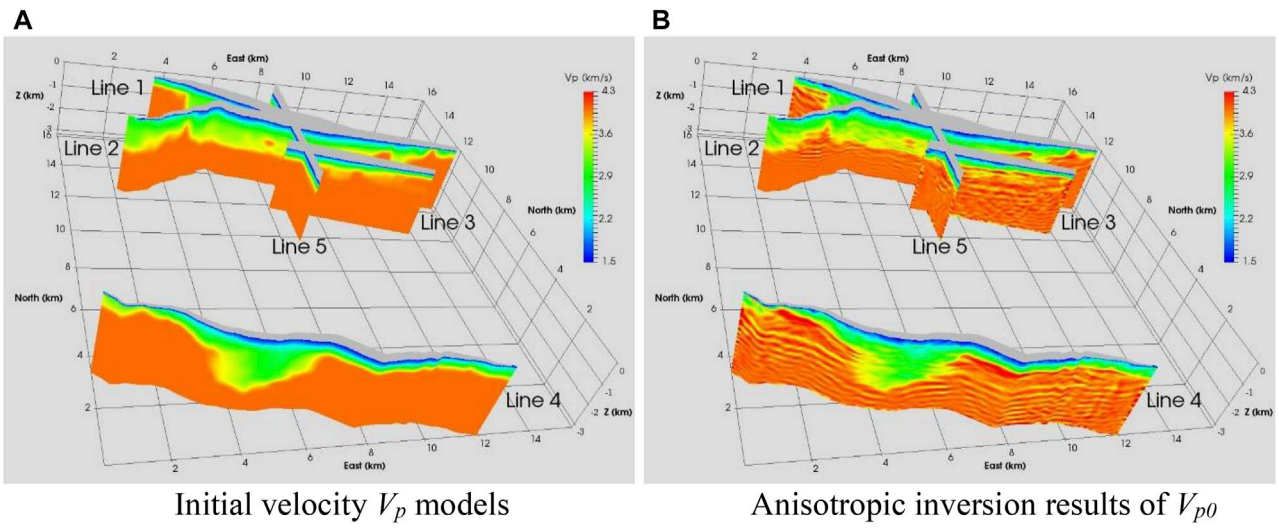

FIGURE 9 | Initial velocity models V_p and anisotropic waveform inversion results of V_{p0} along five 2D lines at Pirouette Mountain and Eleven-Mile Canyon. **(A)** Initial velocity V_p models. **(B)** Anisotropic waveform inversion results of V_{p0}.

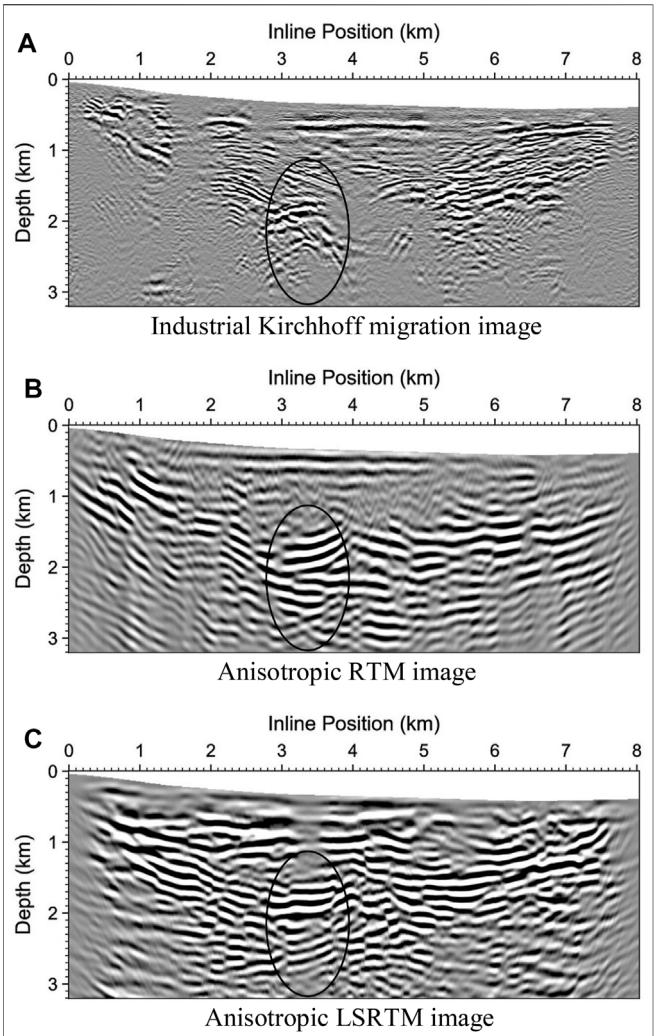

FIGURE 10 | Subsurface migration images of Line 1 at Pirouette Mountain produced using various migration methods: **(A)** Industrial Kirchhoff migration, **(B)** Anisotropic RTM, **(C)** Anisotropic LSRTM. Two nearly-vertical faults can be clearly identified within the ellipse region in **(C)**.

that the slice for the ground-roll noise (red dashed line in **Figure 2**) may also contain signals. This explains the existence of the high-frequency component (above 15 Hz) in the red dashed curve in **Figure 3**. In the low-frequency band, the signal spectrum (blue curve) encroaches on the spectrum of the ground-roll noise. Therefore, a simple low-cut filtering to suppress the ground-roll noise would also filter out some low-frequency component of the signal, while low-frequency data are crucial for full-waveform inversion.

If an input trace is the signal (e.g., of the blue spectral profile in **Figure 3**), we would enforce a wide bandpass filter, e.g., of the blue filtering profile in **Figure 4**. This filter is wide because the low cut-off frequency f_2 is small. On the other hand, if an input trace is the ground-roll noise, we would enforce a narrow bandpass filter, e.g., of the red filtering profile in **Figure 3**. This filter is narrow because the low cut-off frequency f_1 is large. In reality, however, we do not know whether an input trace is signal or ground-roll noise a priori. Fortunately, the wavenumbers in common-shot gathers can indicate the likelihood whether an input trace is the ground-roll noise.

Figure 2 shows that the wavenumber-magnitude $|k_x|$ of the ground-roll noise is smaller than that of the reflection signal, because the apparent horizontal wavelength λ_x of the ground-roll noise is larger than that of the reflection signal. Furthermore, the dipping angles of the narrow 'wavefronts' of the ground-roll noise within the red rectangles are opposite to those of the signal within the cyan rectangle. One can infer whether an input is the ground-roll noise using this wavenumber information. We use this information to design an *f-k* filter as shown in **Figure 5** for suppressing the ground-roll noise.

For seismic traces on the left side of the shot in a common-shot gather, any vertical cross-section of **Figure 5** is a bandpass filter, similar to the profiles in **Figure 4**. When k_x is large, the input should be signal, and therefore, the bandpass filter would have a small low-cut frequency f_2 value. On the other hand, when signed k_x is small, the input should be the ground-roll noise, and therefore, the bandpass filter would have a large low-cut frequency f_1. The k_1 and k_2 values in **Figure 5** define a transition zone between those two bandpass filters. Since the bandpass filter's parameterization changes with respect to wavenumber k_x, we name our filter "the wavenumber-adaptive bandpass filter." For seismic traces on the right side of a shot in a common-shot gather, **Figure 5** is mirror-reflected with respect to the k_x axis.

We use the following procedure to determine parameters of the wavenumber-adaptive bandpass filter:

1) Pick f_2, e.g., 5 Hz, and f_1, e.g., 24 Hz (**Figure 4**).
2) Work on a few common-shot gathers. Enclose regions of ground-roll (G) and reflections (R), e.g., **Figure 2**. Let the objective function $J = e(\mathrm{R}) - e(\mathrm{G})$, where e is average energy.
3) Pick initial values of $k_1 = 0$, $k_2 = 2\pi/\lambda_2$ where $\lambda_2 = 578$ m. Update k_1 and k_2 by maximizing J (**Figure 5**).
4) Construct the F-K filter (**Figure 5**).

Then we use the following procedure to attenuate the ground-roll noise:

1) For a common-shot gather (CSG) with shot s_x, pick the left part where traces $g_x < s_x + margin$.
2) Apply the F-K filter (**Figure 5**) on this left part, to yield AGN1.
3) For this same CSG, pick the right part where traces $g_x > s_x - margin$.
4) Mirror-reflect the F-K filter in **Figure 5**; namely $k_x \leftarrow -k_x$.
5) Apply this mirror-reflected F-K on the right part, to yield AGN2.
6) Merge AGN1 and AGN2; use a cosine interpolation weight in their overlapping regions.

Anisotropic Least-Squares Reverse-Time Migration

Least-squares reverse-time migration (LSRTM) seeks to improve a reflectivity model m over iterations, by minimizing a least-squares data residue J defined as

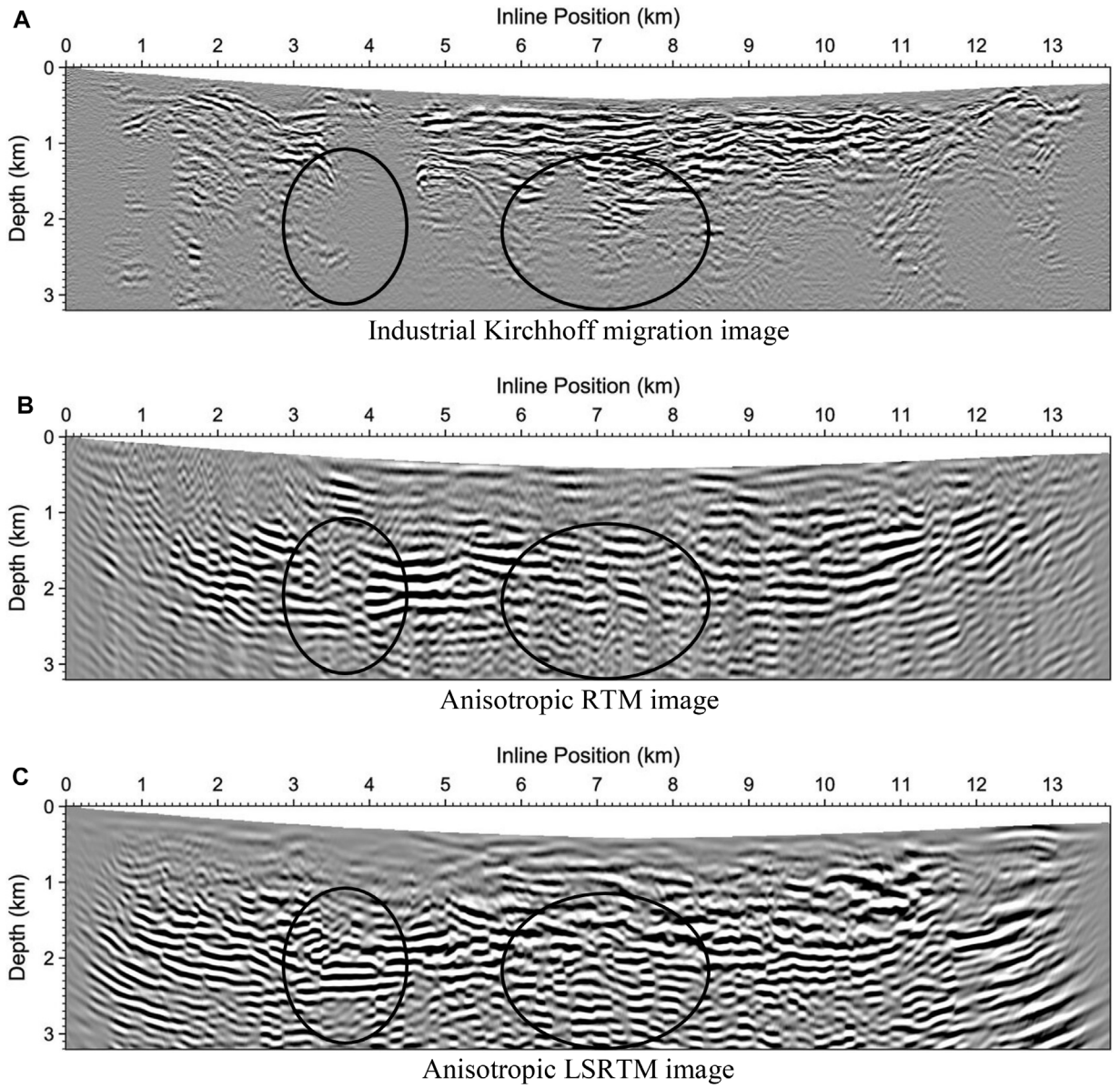

FIGURE 11 | Subsurface migration images of Line 2 at Pirouette Mountain produced using various migration methods: **(A)** Industrial Kirchhoff migration, **(B)** Anisotropic RTM, **(C)** Anisotropic LSRTM. The images within the ellipse regions in **(C)** are much better than those in **(B)**, and are not imaged in **(A)**.

$$J = \frac{1}{2} \parallel \mathbf{d} - \mathbf{Lm} \parallel_2^2, \tag{1}$$

where **d** represents observed seismic data, and operator **L** is the Born modeling operator. The Born modeling operator is based on the full-wavefield propagator. For 2D tilted transversely isotropic (TTI) media, we adopt a decoupled qP-wave equation to describe the qP-wave propagation (Zhan et al., 2012):

$$\frac{1}{V_{p0}^2} \frac{\partial^2 P}{\partial t^2} = \nabla_{\text{aniso}}^2 P, \tag{2}$$

where the spatial Laplacian ∇_{aniso}^2 for acoustic TTI media is

$$\nabla_{\text{aniso}}^2 = -\left\{ \begin{array}{l} k_x^2 + k_z^2 \\ + \left(2\varepsilon \cos^4\theta + 2\delta \sin^2\theta \cos^2\theta\right) \frac{k_x^4}{k_x^2 + k_z^2} + \left(2\varepsilon \sin^4\theta + 2\delta \sin^2\theta \cos^2\theta\right) \frac{k_z^4}{k_x^2 + k_z^2} \\ + \left(-4\varepsilon \sin 2\theta \cos^2\theta + \delta \sin 4\theta\right) \frac{k_x^3 k_z}{k_x^2 + k_z^2} + \left(3\varepsilon \sin^2 2\theta - \delta \sin^2 2\theta + 2\delta \cos^2 2\theta\right) \frac{k_x^2 k_z^2}{k_x^2 + k_z^2} \end{array} \right\} \tag{3}$$

where V_{p0} is the qP-wave velocity along the TTI symmetry axis; k_x and k_z are the spatial wavenumbers in the x and z directions, respectively; ε and δ are the Thomsen parameters (Thomsen, 1986), where ε describes the difference between the qP-wave velocities perpendicular to and parallel with the TTI symmetry

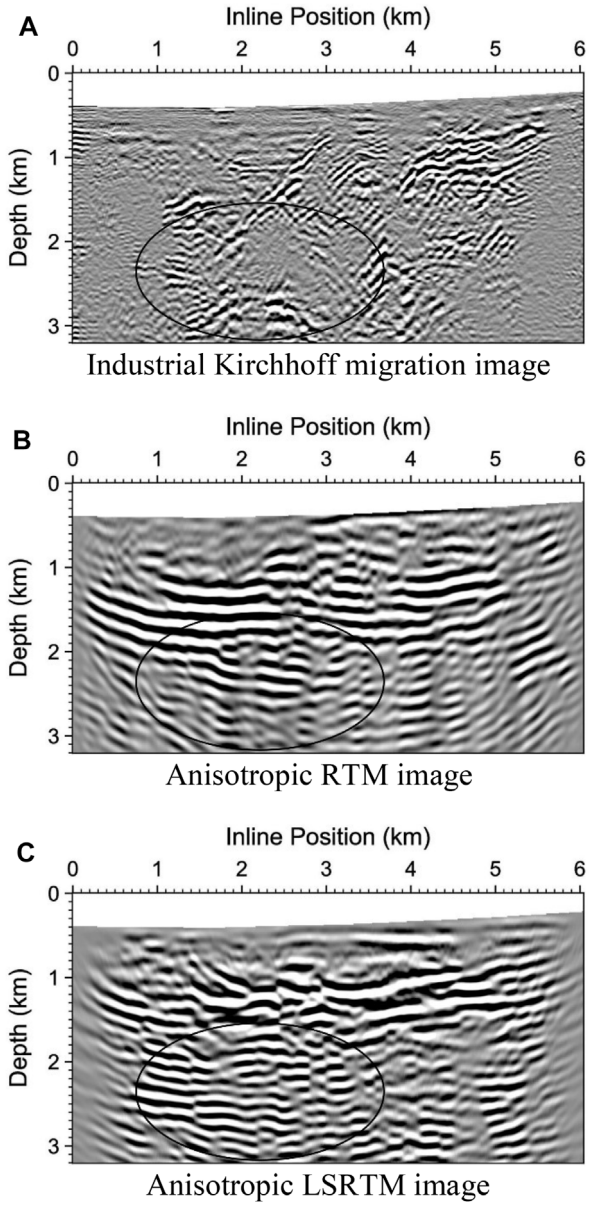

FIGURE 12 | Subsurface migration images of Line 3 at Pirouette Mountain produced using various migration methods: **(A)** Industrial Kirchhoff migration, **(B)** Anisotropic RTM, **(C)** Anisotropic LSRTM. The image within the ellipse region in **(C)** has higher resolution than that in **(B)**, and is imaged very poorly in **(A)**.

axis (i.e., the long offset effect), δ describes the near-symmetry-axis qP-wave velocity variation (i.e., the short offset effect), and θ is the tilt angle of the TTI symmetry axis.

To minimize the misfit functional J, $\mathbf{m}$ is updated iteratively through

$$\begin{aligned}\mathbf{m}^{(k+1)} &= \mathbf{m}^{(k)} - \alpha^{(k)}\nabla_{\mathbf{m}}J \\ &= \mathbf{m}^{(k)} + \alpha^{(k)}\mathbf{L}^{\mathrm{T}}\left(\mathbf{d} - \mathbf{L}\mathbf{m}^{(k)}\right),\end{aligned} \tag{4}$$

where the superscripts (k) and $(k+1)$ denote the k^{th} and $(k+1)^{\mathrm{th}}$ iteration, respectively, and $\alpha^{(k)}$ denotes the step length at the k^{th} iteration. Note that when $m^{(k)} = 0$ at the second line of **Eq. (4)**, the line is proportional to $L^{\mathrm{T}}0$, which is considered as the image of RTM. Therefore, RTM is merely the first iteration of LSRTM when starting from $m^{(0)} = 0$.

The gradient term $\mathbf{L}^{\mathrm{T}}(\mathbf{d} - \mathbf{L}\mathbf{m})$ is equivalent to computing an imaging condition as in reverse-time migration by migrating the data residue $(\mathbf{d} - \mathbf{L}\mathbf{m})$. To more accurately form this imaging condition free of low-wavenumber artifacts, we implement this step as below:

$$\begin{aligned}G_{\mathrm{pp,down}}(\mathbf{x}) &= \sum_{N_s,N_r}\int_0^T [P_sP_r - H_z(P_s)H_z(P_r) - P_sH_z(H_t(P_r)) \\ &\quad - H_z(P_s)H_t(P_r)]dt, \\ G_{\mathrm{pp,left}}(\mathbf{x}) &= \sum_{N_s,N_r}\int_0^T [P_sP_r - H_x(P_s)H_x(P_r) + P_sH_x(H_t(P_r)) \\ &\quad + H_x(P_s)H_t(P_r)]dt, \\ G_{\mathrm{pp,right}}(\mathbf{x}) &= \sum_{N_s,N_r}\int_0^T [P_sP_r - H_x(P_s)H_x(P_r) - P_sH_x(H_t(P_r)) \\ &\quad - H_x(P_s)H_t(P_r)]dt,\end{aligned} \tag{5}$$

where $G_{pp,\bullet}$'s are gradients associated with the directional PP images; P is the pure qP-wavefield, and subscripts $s$and r represent the source and receiver, respectively; and H_x, H_z and H_t represent the Hilbert transforms in the horizontal direction, vertical direction, and time domain, respectively.

To produce more reliable and high-resolution images when the observed data are noisy, irregular, and sparse, we employ a modified total-variation regularization scheme (Gao et al., 2015; Lin and Huang, 2015) to improve the convergence and imaging fidelity. The misfit function in **Eq. (1)** becomes

$$J(\mathbf{m},\mathbf{u}) = \min_{\mathbf{m}}\left\{\min_{\mathbf{u}}\left\{\frac{1}{2}\|\mathbf{d} - \mathbf{L}\mathbf{m}\|_2^2 + \lambda_1\|\mathbf{m} - \mathbf{u}\|_2^2 + \lambda_2\|\mathbf{u}\|_1^1\right\}\right\}, \tag{6}$$

where λ_1 and λ_2 are regularization parameters. We solve this regularized minimization problem using an alternating-direction minimization scheme (Lin and Huang, 2015).

Suppressing the Ground-Roll Noise of Land Surface Seismic Data From Pirouette Mountain and Eleven-Mile Canyon

We apply our novel wavenumber-adaptive bandpass filter to five lines of 2-D seismic data acquired at Pirouette Mountain and Eleven-Mile Canyon for geothermal exploration (**Figure 1**) to suppress the ground-roll noise. As an example of ground-roll noise suppression for the seismic data on Line 1, we depict the results of three common-shot gathers in **Figure 6**. Comparing the second and third columns in **Figure 6**, we find that the ground-roll noise is mostly suppressed in the third column. The

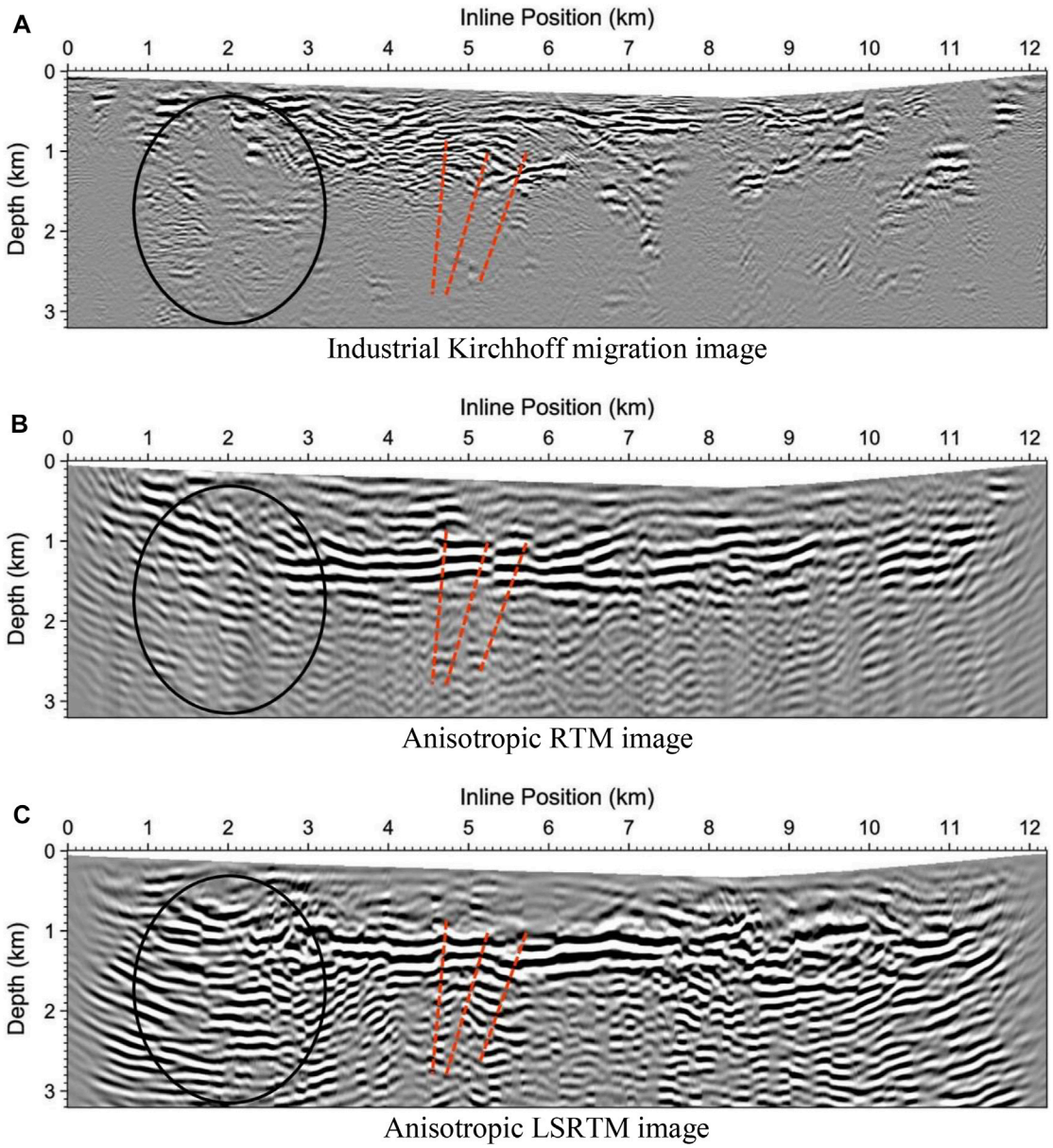

FIGURE 13 | Subsurface migration images of Line 4 at Eleven-Mile Canyon produced using various migration methods: **(A)** Industrial Kirchhoff migration, **(B)** Anisotropic RTM, **(C)** Anisotropic LSRTM. The image within the ellipse region in **(C)** corresponds to the rupture region as shown in **Figure 1**. The image in this region has higher resolution than that in **(B)**, and is almost invisible in **(A)**. The delineated faults in **(C)** may correspond to the faults identified in the U.S. Geological Survey Quaternary fault and fold database as shown in **Figure 1**.

signals within the blue ellipses preserve the low-frequency component.

Figure 7 shows a common-shot gather before and after wavenumber-adaptive bandpass filtering. Some coherent subsurface reflections can be identified on the processed common-shot gather displayed on the right panel of **Figure 7**.

Note that the wavenumber-adaptive bandpass filters used are the same for all common-shot gathers. However, in case the nature of common-shot gathers differs a lot, then it is necessary to determine different values for parameters f_1, f_2, and k_2.

We use the processed data with the ground-roll noise removed to produce subsurface complex structural images using anisotropic RTM and anisotropic LSRTM.

Anisotropic Least-Squares Reverse-Time Migration of Seismic Data From Pirouette Mountain and Eleven-Mile Canyon

After suppressing the ground-roll noise in the surface seismic data along five 2D lines (**Figure 8**) acquired at Pirouette

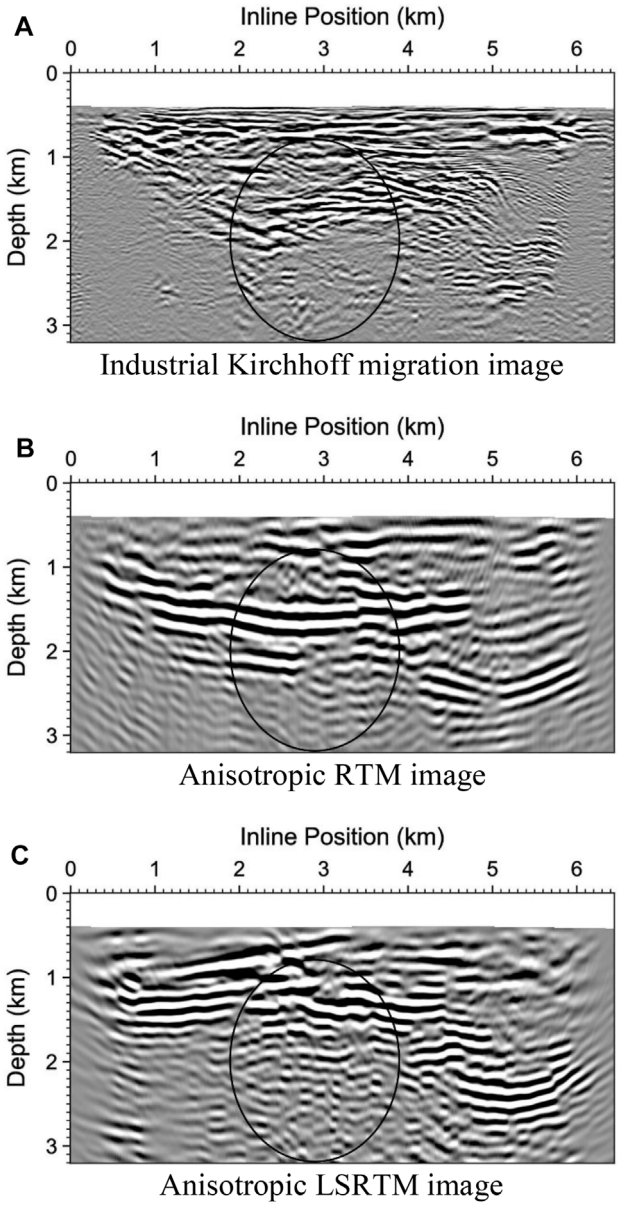

FIGURE 14 | Subsurface migration images of Line 5 at Pirouette Mountain produced using various migration methods: **(A)** Industrial Kirchhoff migration, **(B)** Anisotropic RTM, **(C)** Anisotropic LSRTM. The image within the ellipse region in **(C)** shows high-resolution structures in the deep region that are not well imaged in **(B)** and **(A)**.

Mountain and Eleven-Mile Canyon, we apply anisotropic LSRTM to the resulting data, and compare our imaging results with industrial Kirchhoff migration images and those of anisotropic RTM. We carry out necessary preprocessing steps, such as converting the phase of the seismic data from 3D to 2D because we perform migration imaging in 2D, in addition to the ground-roll noise removal. For anisotropic RTM and anisotropic LSRTM, we first obtain a velocity model and anisotropic parameters $(V_{P0}, \varepsilon, \delta, \theta)$ using multi-scale anisotropic full-waveform inversion with total generalized p-variation regularization (Gao and Huang 2019). Our full-waveform inversion starts from a low-frequency band and an initial velocity model obtained using refraction traveltime tomography to produce reliable models of anisotropic parameters. **Figure 9** shows the initial velocity V_p models along the five seismic survey lines at Pirouette Mountain and Eleven-Mile Canyon obtained using refraction tomography, and our anisotropic waveform inversion results of V_{p0}.

Figures 10–14 show images of the industrial Kirchnoff migration, anisotropic RTM, and anisotropic LSRTM, for seismic survey Lines 1–5. Both anisotropic RTM and anisotropic LSRTM images outperform the industrial images, and anisotropic LSRTM outperforms anisotropic RTM. Kirchhoff migration generates poor images, and particularly in the deep regions. Anisotropic LSRTM produces images with higher resolution, particularly in the deep region and the regions near both end of each line, than anisotropic RTM.

As shown within the ellipse regions in **Figure 10** for Line 1, two steeply-dipping faults can be clearly identified on the anisotropic LSRTM image, which cannot be easily recognized on the anisotropic RTM image, and are invisible on the Kirchhoff migration image.

Figure 11 shows that anisotropic LSRTM reveals more structures in the deep region along Line 2. For example, the images within the ellipse regions in the anisotropic LSRTM image depicted in **Figure 11C** are much better than those of anisotropic RTM in **Figure 11B**, and are not imaged by Kirchhoff migration in **Figure 11A**.

Along Line 3 as shown in **Figure 12**, the image within the ellipse region of the anisotropic LSRTM result in **Figure 12C** has higher resolution than that of anisotropic RTM in **Figure 12B**, and is imaged very poorly by Kirchhoff migration in **Figure 12A**.

The image within the ellipse region in **Figure 13C** along Line 4 obtained using anisotropic LSRTM corresponds to the rupture region as shown in **Figure 1**. The image in this region has higher resolution than that of anisotropic RTM in **Figure 13B**, and is almost invisible in the industrial Kirchhoff migration image in **Figure 13A**. The delineated faults in **Figure 13C** may correspond to the faults identified in the U.S. Geological Survey Quaternary fault and fold database as shown in **Figure 1**.

Line 5 cuts through Lines 1-3 along the North-South direction. The image within the ellipse region of the anisotropic LSRTM image in **Figure 14C** shows high-resolution structures in the deep region that are not well imaged in the other two methods shown in **Figures 14A,B**.

Figure 15 displays a comparison between 3D views of industrial Kirchhoff migration (left) and our anisotropic LSRTM migration (right) for the five seismic survey lines at Pirouette Mountain and Eleven-Mile Canyon. Anisotropic LSRTM reveals high-resolution subsurface images along five seismic survey lines that can be used to identify faults for geothermal exploration.

The final data misfit of anisotropic LSRTM reduces to approximately 50–60% of the initial data misfit after eight iterations. Anisotropic RTM is the first iteration of anisotropic LSRTM. Therefore, our anisotropic LSRTM images are more reliable than those of anisotropic RTM for geothermal exploration.

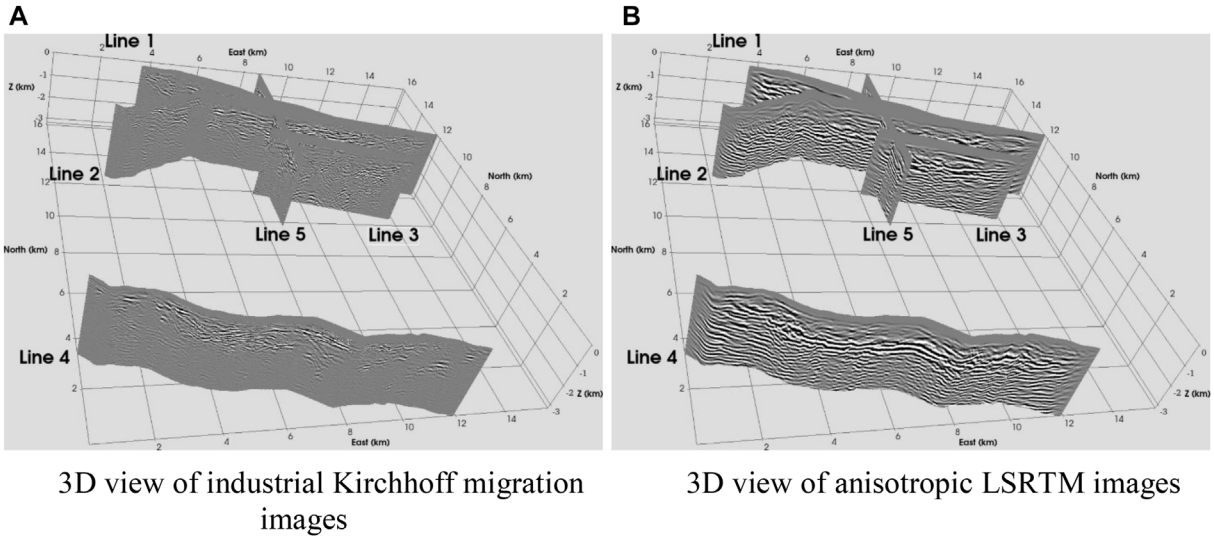

FIGURE 15 | Comparison between 3D views of industrial Kirchhoff migration **(left)** and our anisotropic LSRTM migration **(right)**. Anisotropic LSRTM reveals high-resolution subsurface images along five seismic survey lines at Pirouette Mountain and Eleven-Mile Canyon that can be used to identify faults for geothermal exploration. **(A)** 3D view of industrial Kirchhoff migration images. **(B)** 3D view of anisotropic LSRTM images.

CONCLUSION

We have developed a novel wavenumber-adaptive bandpass filtering method for suppressing the ground-roll noise in land seismic data without filtering out seismic signals. This method employs the fact that the frequency-wavenumber information of the ground-roll noise differs from that of the signal. We have applied our new method to five 2D lines of seismic data acquired at Pirouette Mountain and Eleven-Mile Canyon in Nevada for geothermal exploration, and have successfully suppressed the strong and coherent ground-roll noise. We have applied our anisotropic least-squares reverse-time migration method to the processed seismic data and produced high-resolution subsurface images. Compared with both industrial Kirchhoff migration and anisotropic reverse-time migration, our anisotropic least-squares reverse-time migration improves the subsurface images significantly, both in image resolution and image quality, particularly in the deep region. Our images reveal faults more clearly, some of which are invisible on the other images. This improvement is particularly evidenced by the subsurface images of Line 4, where our image manifests faults consistent with the geology. These results demonstrate that anisotropic least-squares reverse-time migration is an advantageous addition to the state-of-the-art anisotropic reverse-time migration for imaging complex subsurface structures with various faults. Our high-resolution subsurface images at Pirouette Mountain and Eleven-Mile Canyon facilitate accurate fault interpretation for reliable geothermal exploration.

DATA AVAILABILITY STATEMENT

The data analyzed in this study are subject to the following licenses/restrictions: Data are available through the US Navy Geothermal Program Office by contacting co-author AS. Requests to access these datasets should be directed to AS.

AUTHOR CONTRIBUTIONS

YH performed ground-roll suppression and imaging. MZ performed data analyses and anisotropic waveform inversion. KG developed the inversion and imaging codes. AS provided the field seismic data, and performed geologic interpretation. LH was the principal investigator of the research project, obtained funding, provided the research ideas, wrote the paper.

FUNDING

This work was supported by the Geothermal Technologies Office of the U.S. Department of Energy (DOE) through the Los Alamos National Laboratory (LANL), which is operated by Triad National Security, LLC, for the National Nuclear Security Administration (NNSA) of U.S. DOE under Contract No. 89233218CNA000001. This research used resources provided by the LANL Institutional Computing Program, which is supported by the U.S. DOE NNSA under Contract No. 89233218CNA000001.

ACKNOWLEDGMENTS

We thank reviewers YL and BH for their valuable comments.

REFERENCES

Alm, S., Walker, J. D., and Blake, K. (2016). Structural Complexity of the Pirouette Mountain and Elevenmile Canyon Geothermal Systems. *Trans. Geothermal Resour. Counc.* 40, 433–438.

Ba, J., Du, Q., Carcione, J. M., Zhang, H., and Muller, T. M. (2015). *Seismic Exploration of Hydrocarbons in Heterogeneous Reservoirs*. Amsterdam, Netherlands: Elsevier.

Brysk, H., and McCowan, D. W. (1986). A Slant-stack Procedure for point-source Data. *Geophysics* 51 (7), 1370–1386. doi:10.1190/1.1442187

Caskey, S. J., Wesnousky, S. G., Zhang, P., and Slemmons, D. B. (1996). Surface Faulting of the 1954 Fairview Peak (MS 7.2) and Dixie Valley (MS 6.8) Earthquakes, Central Nevada. *Bull. Seismological Soc. America* 86, 761–787. doi:10.1785/BSSA0860030761

Coruh, C., and Costain, J. K. (1983). Noise Attenuation by Vibroseis Whitening (VSW) Processing. *Geophysics* 48 (5), 543–554. doi:10.1190/1.1441485

Deighan, A. J., and Watts, D. R. (1997). Ground-roll Suppression Using the Wavelet Transform. *Geophysics* 62 (6), 1896–1903. doi:10.1190/1.1444290

Embree, P., Burg, J. P., and Backus, M. M. (1963). Wide-band Velocity Filtering-The Pie-slice Process. *Geophysics* 28 (6), 948–974. doi:10.1190/1.1439310

Gao, K., and Huang, L. (2019). Acoustic- and Elastic-Waveform Inversion with Total Generalized P-Variation Regularization. *Geophys. J. Int.* 218, 933–957. doi:10.1093/gji/ggz203

Gao, K., and Huang, L. (2015).Anisotropic Elastic-Waveform Modeling for Fracture Characterization in EGS Reservoirs. Proceedings of the 40th Workshop on Geothermal Reservoir Engineering, CA (United States), 26-28 Jan 2015. Stanford, CA: Stanford University. doi:10.2172/1168705

Halliday, D. (2011). Adaptive Interferometry for Ground-Roll Suppression. *The Leading Edge* 30 (5), 532–537. doi:10.1190/1.3589110

Henley, D. C. (2003). Coherent Noise Attenuation in the Radial Trace Domain. *Geophysics* 68 (4), 1408–1416. doi:10.1190/1.1598134

Jin, S., and Ronen, S. (2005).Ground Roll Detection and Attenuation by 3C Polarization Analysis. Proceedings of the 67th Annual Conference and Exhibition, Madrid, Spain, Jun 2005. Extended Abstracts (Houten, The Netherlands: European Association of Geoscientists & Engineers). doi:10.3997/2214-4609-pdb.1.b020

Karsli, H., and Bayrak, Y. (2008). Ground-Roll Attenuation Based on Wiener Filtering and Benefits of Time-Frequency Imaging. *The Leading Edge* 27 (2), 206–209. doi:10.1190/1.2840368

Lin, Y., and Huang, L. (2015). Acoustic- and Elastic-Waveform Inversion Using a Modified Total-Variation Regularization Scheme. *Geophys. J. Int.* 200, 489–502. doi:10.1093/gji/ggu393

Liu, X. (1999). Ground Roll Supression Using the Karhunen-Loeve Transform. *Geophysics* 64 (2), 564–566. doi:10.1190/1.1444562

Nemeth, T., Wu, C., and Schuster, G. T. (1999). Least-squares Migration of Incomplete Reflection Data. *Geophysics* 64, 208–221. doi:10.1190/1.1444517

Sheriff, R. E. (2002). Encyclopedic Dictionary of Applied Geophysics. *Soc. exploration geophysicists*, 442. doi:10.1190/1.9781560802969

Shieh, C. F., and Herrmann, R. B. (1990). Ground Roll: Rejection Using Polarization Filters. *Geophysics* 55 (9), 1216–1222. doi:10.1190/1.1442937

Thomsen, L. (1986). Weak Elastic Anisotropy. *Geophysics* 51, 1954–1966. doi:10.1190/1.1442051

Trad, D., Ulrych, T., and Sacchi, M. (2003). Latest Views of the Sparse Radon Transform. *Geophysics* 68 (1), 386–399. doi:10.1190/1.1543224

Treitel, S., Shanks, J. L., and Frasier, C. W. (1967). Some Aspects of Fan Filtering. *Geophysics* 32 (5), 789–800. doi:10.1190/1.1439889

Unruh, J., Gray, B., Christopherson, K., Pullammanappallil, S., Alm, S., and Blake, K. (2016). Seismic Reflection and Magnetotelluric Imaging of Southwestern Dixie Valley Basin, Nevada. *Trans. Geothermal Resour. Counc.* 40, 455–461.

Yilmaz, Ö. (2001). Seismic Data Analysis: Processing, Inversion, and Interpretation of Seismic Data. *Soc. exploration geophysicists* 10, 837–1000. doi:10.1190/1.9781560801580

Zhan, G., Pestana, R. C., and Stoffa, P. L. (2012). Decoupled Equations for Reverse Time Migration in Tilted Transversely Isotropic media. *Geophysics* 77, T37–T45. doi:10.1190/geo2011-0175.1

Conflict of Interest: The authors declare that the research was conducted in the absence of any commercial or financial relationships that could be construed as a potential conflict of interest.